Mode Transitions in Hall-Effect Thrusters Induced by Variable Magnetic Field Strength

Michael J. Sekerak* and Alec D. Gallimore†
University of Michigan, Ann Arbor, Michigan 48105
Daniel L. Brown‡
U.S. Air Force Research Laboratory, Edwards Air Force Base, California 93524
and
Richard R. Hofer§ and James E. Polk¶
Jet Propulsion Laboratory, California Institute of Technology, Pasadena, California 91109

Mode transitions in a 6 kW laboratory Hall-effect thruster were induced by varying the magnetic field intensity while holding all other operating parameters constant. Ultrafast imaging, discharge current, and thrust measurements were used to characterize the change in discharge channel current density and thruster performance through mode transitions. The modes are described here as global oscillation mode and local oscillation mode. In global mode, the entire discharge channel is oscillating in unison and spokes are either absent or negligible with discharge current oscillation amplitude (root mean square) greater than 10% of the mean value and can even be as high as 100%. In local oscillation mode, perturbations in the discharge current density are seen to propagate in the $E \times B$ direction. Spokes are localized oscillations that are typically 10–20% of the mean discharge current density value. The discharge current oscillation amplitude and mean values are significantly lower than global mode. The mode transitions changed with operating conditions, where the transition between global mode and local mode occurred at higher relative magnetic field strengths for higher mass flow rate or higher discharge voltage. The thrust was approximately constant through the mode transition, but the thrust-to-power ratio and anode efficiency decreased significantly in global mode. The peaks in thrust to power and anode efficiency typically occur near the transition point. Thruster performance maps should include variation in discharge current, discharge voltage, and magnetic field, known as $I_D - V_D - B$ maps, at different flow rates to identify transition regions throughout the life of a thruster. These results are used to calculate a transition surface for use by operators to keep the thruster operating in an optimal mode.

Nomenclature

A_{ch}	=	area of discharge channel exit plane, m^2
B_r	=	peak radial magnetic field strength on discharge channel centerline, G
B_r^*	=	peak radial magnetic field strength on discharge channel centerline for reference condition, G
B_r/B_r^*	=	normalized magnetic field strength
$B_r/B_r^*\|_{\text{trans}}$	=	normalized magnetic field at mode transition (lower and upper)
$E \times B$	=	direction of electric field crossed with magnetic field
$\bar{I}_D$	=	mean discharge current, A
$\tilde{I}_D$	=	discharge current root mean square, A
$I_{D_{\text{ac}}}(t)$	=	alternating current component of the discharge current time history, A
$I_D(t)$	=	discharge current time history, A
I_{IM}	=	inner magnet current, A
I_{OM}	=	outer magnet current, A
j_D	=	mean discharge channel current density, $mA\ cm^{-2}$
$\bar{j}_D\ j_D(t)$	=	discharge channel current density time history, $mA\ cm^{-2}$
k_B	=	Boltzmann's constant, $j \cdot K^{-1}$
L_{ch}	=	channel length, m
L_i	=	ionization region length, m
m	=	spoke order
$\dot{m}_a$	=	anode mass flow rate, $mg \cdot s^{-1}$
$\dot{m}_a^*$	=	reference anode mass flow rate, $mg \cdot s^{-1}$
$\dot{m}_c$	=	cathode mass flow rate, $mg \cdot s^{-1}$
m_e	=	electron mass, kg
m_i	=	ion mass, kg
m_N	=	neutral mass, kg
n	=	quasi-neutral plasma density, m^{-3}
n_N	=	neutral density, m^{-3}
P_D	=	discharge power, W
$\text{PSD}_{m_{\max}}$	=	peak value of spoke surface power spectral density for m spoke order m
PSD_{m_0}	=	peak value of spoke surface power spectral density for spoke order m_0
q	=	elementary charge, C
R_i	=	discharge channel inner radius, m
R_o	=	discharge channel outer radius, m
T	=	thrust, N
T_N	=	neutral temperature, K
T/P	=	thrust to power, $mN\ kW^{-1}$
V_D	=	discharge voltage, V
V_D^*	=	reference discharge voltage, V
$v_{E \times B}$	=	$E \times B$ drift velocity, $m \cdot s^{-1}$
v_i	=	ion velocity, $m \cdot s^{-1}$
v_{th_N}	=	neutral thermal velocity, $m \cdot s^{-1}$

W_{ch}	=	discharge channel width, m
η_a	=	anode efficiency
η_V	=	voltage utilization efficiency
ν_{ef}	=	effective collision frequency, s^{-1}
Ψ	=	coefficient

I. Introduction

HALL-EFFECT thrusters (HETs) have been under development for over 50 years in Russia [1] and the United States with significant experimental and flight histories. Mode transitions have been commonly observed throughout their development as noted by some of the early pioneering Russian research [2]. HETs have several parameters that define a single operating point, such as discharge voltage, magnetic field strength (or magnet coil current), anode mass flow rate, and cathode mass flow rate. Laboratory HET discharge power supplies typically operate in voltage regulated mode, where the discharge voltage between the anode and cathode is held constant and the discharge current is allowed to fluctuate. Generally, mode transitions are identified by changes in the discharge current characteristics, including mean value and oscillation amplitude. Mode transitions can be caused by changes in discharge voltage, anode mass flow rate, cathode mass flow rate, magnetic field magnitude and/or shape, wall shape due to erosion, wall properties due to release of absorbed compounds or deposition, ambient neutral density in the near-field plume region between the cathode and discharge channel, cathode location, and deposition/oxidation on the anode. Note that changes in the magnetic field can be intentionally induced by changing the electromagnetic coil currents or unintentionally caused by degradation of the magnetic circuit or changes in the environment local to the thruster. This investigation uses a well-characterized 6 kW HET called the H6 to study mode transitions by varying magnetic field strength for various operating conditions. Ultrafast imaging and discharge current measurements are used to identify mode transitions. The discharge current, discharge channel current density, and thruster performance changes due to mode transitions are characterized. The modes are defined as global oscillation mode and local oscillation mode with the transition criteria quantified. Development of $I_D - V_D - B_r$ maps is discussed with recommendations for thruster characterization.

II. Definition of Mode Transition

The most detailed delineation of operational modes for varying magnetic field strength was conducted by Tilinin [2], where six regimes were identified as shown in Fig. 1. These definitions were developed using an older stationary plasma thruster (SPT)-type thruster almost 40 years ago and the term "loop" oscillations refer to what are currently called breathing mode oscillations.

1) Collisional (classical) conductivity refers to the weak magnetic field that causes the electron Larmor radius to be comparable to the effective dimensions of the channel and coulomb collisions explain conductivity.

2) The regular electron drift wave is dominated by an azimuthal drift wave that propagates at ~ 0.4–$0.8 v_{E \times B}$.

3) Transition refers to moderate amplitude loop oscillations due to poor conductivity in the discharge channel.

4) Optimal operation occurs when discharge current and loop oscillations are minimized. The electron drift wave is detectable, but of lower amplitude.

5) Macroscopic instability refers to when discharge current abruptly increases and loop oscillations become strong, with visible instabilities in the thruster. Drift waves are absent.

6) Magnetic saturation occurs when discharge is again stabilized and loop oscillations are minimized.

An investigation into mode transitions was done by Tamida et al. for a laboratory Hall thruster based on an SPT design [3] where four regions of oscillation were observed. Two transition lines were identified within the parameter space of discharge voltage V_D, anode mass flow rate $\dot{m}_a$, and magnetic field B_r, which were the classical diffusion transition line of $V_D \dot{m}_a / B_r^2 = \text{const}$ and Bohm diffusion transition line of $V_D / B_r = \text{const}$. An investigation into the operational modes of an SPT-100ML was performed by Béchu et al. in which four different modes were identified by varying discharge voltage [4]. The modes shown by Béchu et al. ([4] Fig. 6) have names that qualitatively describe the discharge current signal shape: irregular mode (100 V), fluctuating mode (300 V), oscillating mode (400 V), and pulsed mode (600 V). An ATON-type thruster called the A53 was developed by the SNECMA and used for characterization testing [5]. ATON thrusters are magnetic layer thrusters, but the gas is injected into a buffer chamber behind the anode instead of the anode acting as the gas distributor. The magnetic field shape is also different, with a magnetic null point in the center of the channel cross section. This thruster has an external cathode similar to the SPT-100. By changing the magnetic coil currents to change the magnetic field strength, two different modes were induced called "spike" mode and "swallow tail" mode [5]. The names for these modes are inspired by the shape of the plume, as shown by Roche et al. ([6] Fig. 9).

A general description of where a mode transition occurs is the point where a sharp discontinuity is observed in the mean discharge current, discharge current oscillation amplitude, and plasma oscillations while varying one parameter and maintaining all others constant. More recent studies have identified two primary operational modes [7–11]. In one mode, the discharge current oscillation amplitude is small with respect to the mean discharge current value, whereas after the mode transition, the mean discharge current rises sharply, as well as the oscillation amplitude. This is demonstrated by the investigations of the H6 operating at low discharge voltages where the two modes are labeled "high-current" and "low-current" modes [9,10]. The body of work on mode transitions suggests wall effects or the plume physics in the region immediately downstream of the discharge channel exit (near-field plume) influence mode transitions. Although the mode transitions are likely a combination of these two factors along with others not yet proposed, investigating the plasma oscillations during mode transition offers insight into the underlying mechanisms. Additional theoretical insight comes from a recent perturbation analysis [12], suggesting that mode transitions represent excitation or damping of ionization oscillations resulting from the balance of heavy species transport and electron energy.

These operational mode investigations and classifications are useful and underscore the importance of understanding the oscillatory characteristics of HETs. As noted by Zhurin et al. [13]: "oscillations at conditions of otherwise poor electron mobility provides the necessary electric conductivity for operation." However, modern HETs, such as the H6 used in this investigation, have benefitted from a half century of research, development, and flight history that has improved magnetic field topology, magnetic circuit design, and anode design. In addition, significant advancements have been made in the field of high-speed diagnostics due to advances in electronics, allowing detailed measurements of plasma oscillations. All factors combined, a renewed investigation into oscillations and
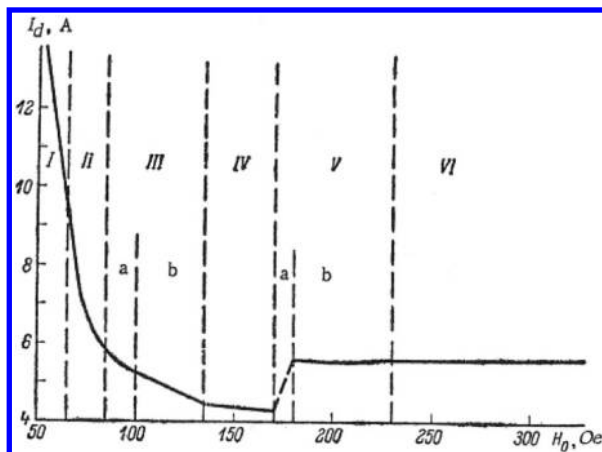
Fig. 1 Discharge current as function of magnetic field with constant discharge voltage showing operational regimes defined by Tilinin [2] (reproduced from [2] Fig. 5).

operational modes using the latest advancements in time-resolved measurements is warranted and presented here.

III. Experimental Setup

A. Introduction

The H6 HET was used to study mode transitions by varying magnetic field strength for various operating conditions. High-speed diagnostics including ultrafast imaging and discharge current measurements provide valuable insight into plasma oscillation changes during mode transitions.

B. Test Facility and Diagnostics

This investigation was conducted in the large vacuum test facility (LVTF) of the Plasmadynamics and Electric Propulsion Laboratory. The LVTF is a 200 m³ stainless-steel-clad vacuum chamber, 9 m long and 6 m in diameter. Rough vacuum is achieved with two 57 m³/min (2000 ft³/min) blowers backed by four 11 m³/min (400 ft³/min) mechanical pumps with a final base pressure in the low 10^{-7} torr achieved by seven CVI TM-1200 reentrant cryopumps with LN₂ baffles and a nominal pumping speed of 500,000 l/s on air or 245,000 l/s on xenon. During thruster operation, the chamber pressure is measured with a Varian 564 external ion gauge mounted at the top of the LVTF above the thruster (~3 m away). The gauge is controlled by a Varian XGS-600 and the pressure measurement uncertainty was estimated to be 20% [14]. Pressure varied for conditions based on anode flow rate but with a fixed chamber pumping speed. The xenon corrected chamber pressures were 8.5×10^{-6}, 1.1×10^{-5}, and 1.4×10^{-5} torr for 14.7, 19.5, and 25.2 mg/s anode flow rate, respectively.

Discharge voltage and current to the thruster were supplied with an Amrel 100 kW dc power supply with a discharge filter consisting of two 220 μF capacitors in parallel. Telemetry, including mean discharge current, cathode-to-ground voltage, discharge voltage, inner and outer magnetic coil currents, and voltages were measured at 1 s intervals with an Agilent 34970A data logger and recorded on a computer using Agilent Benchlink software. The discharge voltage V_D was measured using sense lines on the anode and cathode. Sense line raw voltage signals were sent to a 10,000:1 voltage divider that was calibrated with a BK Precision 5491A multimeter. Mean discharge current $\bar{I}_D = \langle I_D(t) \rangle$, where $\langle \rangle$ denotes the average, was measured with an NT-50 FW Bell sensor. Magnet coil currents were measured with 10 mΩ shunt resistors. All currents were calibrated using a precision 10 mΩ resistor accurate to 0.1% and a BK Precision 5491A multimeter.

Xenon gas (research grade 99.999% pure) was used for the anode and cathode for all testing. The xenon propellant is delivered to the HET using Alicat Scientific MC series mass flow controllers through electropolished stainless steel lines. Mass flow calibration takes place through a Bios Definer 220L DryCal system plumbed in parallel to the anode and cathode feed lines with a measurement accuracy of 1% of the reading between 5 and 500 standard cm³/min. Mass flow calibrations are taken for each mass flow controller at several flow rates and a linear fit is used to determine the flow produced at any arbitrary set point. The ac component of the thruster discharge current $I_{D_{ac}}(t)$ was measured either with a Tektronix TCP 312 (dc to 100 MHz bandwidth) or TCP 303 (dc to 15 MHz bandwidth) split-core Hall current sensors through a Tektronix TCPA 300 current probe amplifier. The signal was measured on the discharge current line external to the chamber on the anode side, using a digital data acquisition system consisting of eight channels sampled at 180 MHz with 16 bit AlazarTech ATS9462 digitizers.

The total discharge current, time history signal is the combination of the two measurements

$$I_D(t) = \bar{I}_D + I_{D_{ac}}(t) \tag{1}$$

Discharge current oscillation amplitude will be defined here as the root mean square of the ac component of the discharge current time history signal in amperes:

$$\tilde{I}_D = \sqrt{\langle (I_D(t) - \bar{I}_D)^2 \rangle} = \sqrt{\langle I_{D_{ac}}(t) \rangle^2} \tag{2}$$

Note that Eq. (2) is the square root of the sample variance for a sample size N and not the square root of the bias-corrected variance, which would have $\sqrt{N-1}$ in the denominator. The difference is negligible for the discharge current signal where the sample size N is between 1×10^6 and 45×10^6 points. The relative discharge current oscillation amplitude is the rms value fraction of the mean discharge current $\tilde{I}_D / \bar{I}_D$. Discharge current density average $\bar{j}_D$ and time history $j_D(t)$ values are defined as

$$\bar{j}_D = \frac{\bar{I}_D}{A_{ch}} \tag{3}$$

$$j_D(t) = \frac{I_D(t)}{A_{ch}} = \frac{\bar{I}_D + I_{D_{ac}}(t)}{A_{ch}} \tag{4}$$

where $A_{ch} = \pi(R_o^2 - R_i^2) = 2\pi R_{ch} W_{ch}$ is the area of the discharge channel with outer and inner radius R_o and R_i, respectively. R_{ch} is the mean channel radius and W_{ch} is the channel width.

The thrust stand is an inverted pendulum based on the NASA Glenn Research Center design of Haag [15] to measure thruster performance. This design has extensive heritage for testing electric propulsion devices [16–18]. In summary, the inverted pendulum thrust stand operates in null mode using a proportional integral derivative (PID) controller and a solenoid actuator to maintain the pendulum in a vertical position based on feedback from a linear variable differential transformer. The thrust stand tilt must remain constant throughout operation, which can shift during pumpdown and thruster operation due to thermal expansion of structural components. An inclinometer is used to monitor thrust stand tilt, and manual adjustments are made with a control motor as necessary. A cooling loop with glycol powered by a Polyscience Durachill 6860T chiller with 5.2 kW cooling capacity is used to thermally regulate the thrust stand. The thruster was operated for over 3 h before any data were acquired in order for the thruster and thrust stand to reach thermal equilibrium. Even if the thrust stand were not at complete thermal equilibrium, this is accounted for by taking zero values at regular intervals where the thruster is briefly turned off and the zero output is recorded. The thrust stand was calibrated by lowering and raising a series of high-precision weights to ensure a linear response. Calibration was performed before thruster operation, two times during testing when the thruster was briefly turned off, and once again after testing was complete. All calibrations showed a linear response and were combined to generate the thruster calibration curve to convert PID controller output in volts to thrust in milliNewtons.

C. H6 Thruster

The H6 Hall thruster shown in Fig. 2 is a 6 kW class Hall thruster with a nominal design voltage of 300 V. The cathode flow fraction is 7%, which is the mass flow rate of gas through the cathode divided by the mass flow rate of gas through the anode $\dot{m}_c / \dot{m}_a$. It uses a hollow cathode with a lanthanum hexaboride (LaB⁶) insert, which can either be mounted centrally (on thruster centerline, which is the nominal configuration) or mounted externally. The inner magnet coil is one continuously wound solenoid core, whereas the outer coil consists of eight discrete solenoid cores wound in series and separated by 45 deg. The outer pole is designed such that inside the discharge channel the magnetic field shown in Fig. 2 (right) is azimuthally uniform to less than 1 G. The H6 is notable for its high total efficiency, for example, 64% at 300 V (6 kW) with a specific impulse of 1950 s, and 70% at 800 V (6 kW) with a specific impulse of 3170 s [19].

Work by Reid [16], Shastry [17], Huang [20], and McDonald [21] studied H6 operation between 5 and 30 mg/s anode flow rates, but primarily focused on 20 mg/s for ~6 kW operation at 300 V. Work by Hofer et al. [22] tuned the flow rate to achieve an integer value for
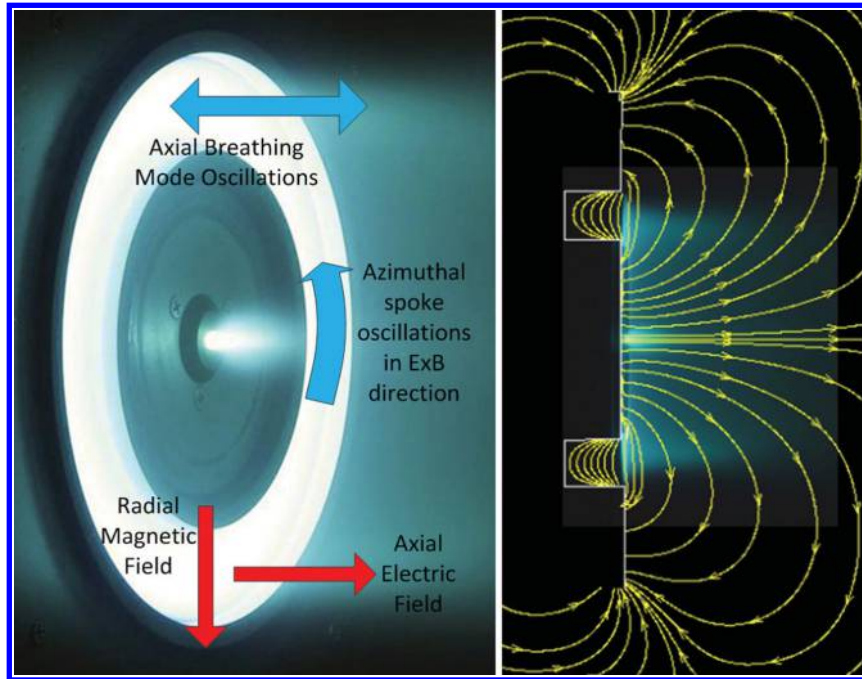
Fig. 2   Picture of H6 (left) with direction of magnetic field and $E \times B$ shown, and (right) operating at nominal conditions with magnetic field streamlines overlaid and discharge channel outlined.

discharge current and power levels (i.e., 20 A for exact 6 kW operation at 300 V). For xenon, these operating conditions vary only by a few percent in current or mass flow rate (1 mg/s Xe ~1 A discharge current), but peak magnetic field strengths between the two cases may vary by up to 15%. At the 300 V, 20 mg/s, 6.1 kW operating condition, the H6 has a 20.3 A discharge current and produces 397 mN of thrust at a specific impulse of about 1900 s [16]. At the nominal 300 V, 20 A, 6 kW condition, the specific impulse is 1950 s with a thrust of 401 mN [19]. The flow rate of 19.5 mg/s is the nominal setting used for comparison in this work and the cathode flow fraction of 7% was maintained for all conditions. The H6 is a well-characterized HET with multiple references for steady-state values and provides an ideal platform for high-speed investigations of oscillatory plasma phenomena.

The magnetic field shape shown in Fig. 2 (right) was kept constant during testing, though the magnitude, noted by B_r/B_r^*, was varied throughout the testing to induce a mode change within the H6. The quantity B_r/B_r^* is the maximum radial magnetic field value at a particular setting of inner magnet I_{IM} current and outer magnet I_{OM} current ($I_{IM}/I_{OM} = 1.12$) divided by the reference maximum radial magnetic field. The reference magnetic field B_r^* strength at 300 V and 20 A discharge current was $I_{IM} = 3.50$ A and $I_{OM} = 3.13$ A, which maximizes total efficiency according to Hofer [22]. This magnetic field strength was used as the nonmagnetically shielded thruster baseline to compare with a magnetically shielded thruster equivalent during their initial development [19,22]. Therefore, this setting has been well characterized and will be considered the reference magnetic field strength.

To confirm the magnetic field magnitude was varied and not topology, magnetic field simulations of the H6 were performed using MagNet Version 7.4.1.4 (32 bit) from Infolytica Corporation for all magnet settings used during magnetic field sweeps. The peak magnetic field value varied linearly with inner magnet current from the minimum of 1.45 A to approximately the reference setting of 3.5 A. However, a second-order least-squares fit best represents the peak magnetic field value across the range of magnet coil currents used:

$$B_r/B_r^* = -0.0105 * I_{IM}^2 + 0.3341 * I_{IM} - 0.0444 \qquad (5)$$

This captured the deviation from linearity for the peak magnetic field that occurred for $I_{IM} \gtrsim 3.5$ A. In practice, deviations in the magnetic

lens symmetry for the H6, which is an important assumption in this investigation, begins at $I_{IM} \sim 4.5$–5.0 A. The axial location of the peak magnetic field did not change to within the 2 mm grid used in simulations. Based on the internal measurements of Reid [16], most of the ionization and acceleration occurs within the axial region approximately $\pm L_{ch}/4$ from the exit plane. Within $\pm L_{ch}/4$ axial distance of the exit plane, the magnetic field direction in the discharge channel was constant for the entire range of magnet current to within 0.5 deg on channel centerline and 2 deg at the walls. Therefore, the magnetic field shape shown in Fig. 2 can be considered constant throughout sweeps and the resulting mode transitions are due solely to the magnitude change. This conclusion will be further supported by the fact that mode transitions across different operating conditions do not occur at any one preferential magnetic field setting.

D.   Test Matrix

Table 1 shows the test matrix for the H6 used in this investigation where a B-field "sweep" is varying magnetic field magnitude with constant flow rate and discharge voltage. Discharge voltages of 300, 400, and 450 V were applied between the anode and cathode. Propellant mass flow rates tested were 25.2, 19.5, and 14.7 mg/s through the anode and 1.8, 1.4, and 1.0 mg/s (7% cathode flow fraction) through the LaB$_6$ cathode. The flow rate of 19.5 mg/s is the nominal setting used for comparison in this work and the cathode flow fraction of 7% was maintained for all conditions.

E.   High-Speed Imaging Analysis

A technique was developed by McDonald et al. [21,23–25] to investigate azimuthal oscillations from videos. In [26], Sekerak adapts the McDonald technique to transform the videos into measurements of discharge current density distribution in the discharge channel to quantify oscillations. These techniques will be referred to as high-speed imagining analysis (HIA) throughout the following discussion.

High-speed images were acquired with a Photron SA5 FastCam with a Nikon ED AF Nikkor 80-200 mm lens at its maximum aperture $f2.8$. The SA5 was used at 87,500 frames/s with 256×256 pixel resolution for this investigation, which yielded approximately 1 mm resolution of the discharge channel. The camera was 6 m downstream from the thruster outside LVTF with a view of the thruster through an optical viewport without filters. In Fig. 3, three monochromatic
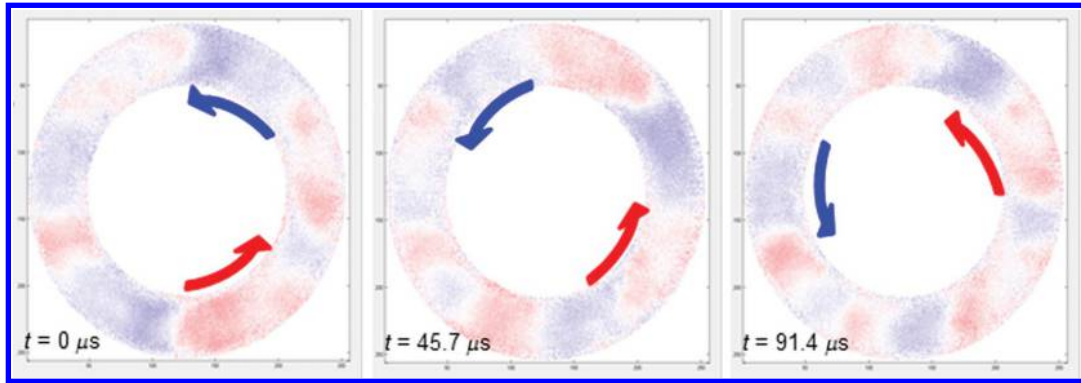
Fig. 3 Three false-colored FastCam frames 45.7 μs apart from a seven frame series showing azimuthal spoke propagation. Red are bright regions (spokes) and blue are dim regions of the discharge channel (reproduced from [27] Fig. 2).
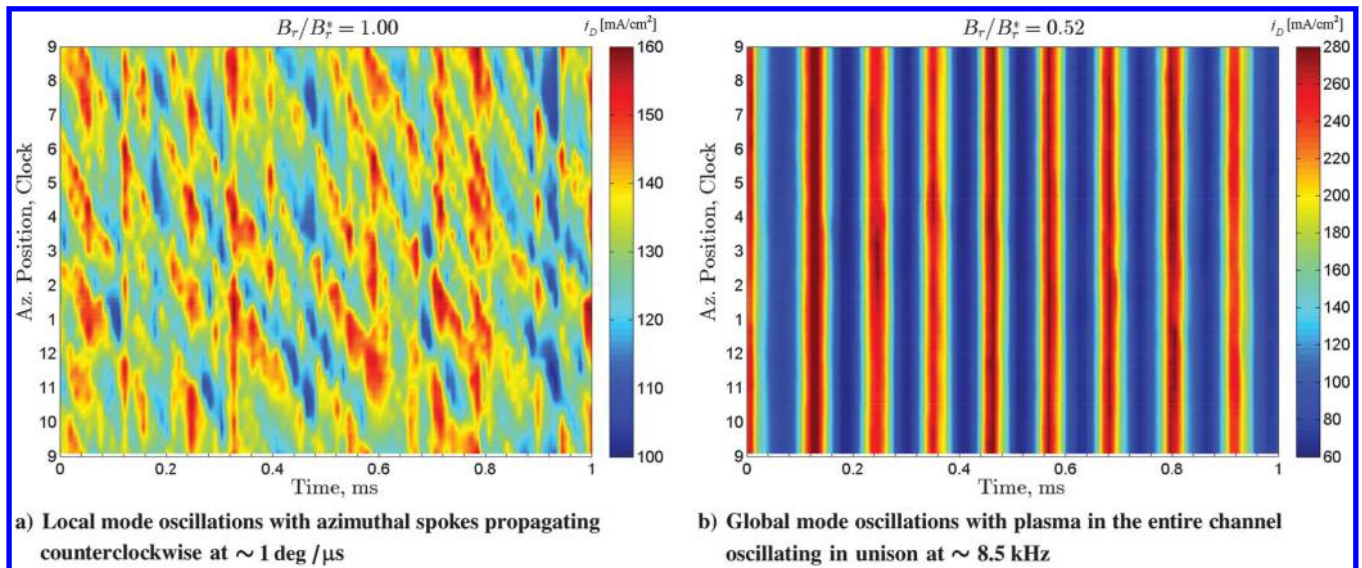

Fig. 4 Example discharge current density plots for two different oscillatory modes. Time segments of 1 ms areas shown at 300 V, 19.5 mg/s operating condition for magnetic field strengths of a) $B_r/B_r^* = 1.00$ and b) $B_r/B_r^* = 0.52$.

FastCam frames 45.7 μs apart have been enhanced with false colors to emphasize the azimuthally propagating spokes in the discharge channel. FastCam frames are every 11.4 μs with the frame rate of 87.5 kHz, so that there are two frames between each of the frames shown. The spokes are coherent bright regions that can be tracked in each frame and move approximately 45 deg in ~45 μs, which corresponds to an angular velocity of ~1 deg/μs and an approximate spoke velocity of ~1400 m/s. Spokes are always observed to propagate in the $E \times B$ direction, even though they do not propagate at the $E \times B$ drift velocity [27].

Details of the McDonald technique are given in [23,26], but a brief summary is provided here. The monochromatic video is imported into MATLAB (MathWorks, Inc.), where each frame is a 256×256 matrix of light intensity values and the dc component is subtracted individually from each pixel. The discharge channel is isolated and divided into 180 2 deg bins. The pixels in each bin are averaged together generating a 180×1 vector of light intensity for each frame. A two-dimensional (2-D) plot of all frames is called the "spoke surface" where the ordinate is azimuthal location around the discharge channel in clock positions and the abscissa is time with each vertical column of values, representing one frame of video. Adding all bins together yields the $m = 0$ or m_0 mode and was first shown by Lobbia et al. [28] to linearly correlate to the discharge current. The same strong linear correlation is also observed in this investigation and is used as the basis for converting light intensity to discharge current density with several assumptions. The most important assumption is that local discharge current density is linearly related to local light intensity, which is supported by the hybrid-direct kinetic simulations of Hara et al. [29]. According to the

simulations, the assumption is valid across similar mode transitions as those observed in this work.

As detailed in [26,27], the spoke surface or discharge current density surface yields valuable information on plasma oscillations within the discharge channel by showing the time-resolved azimuthal distribution of light intensity. Examples of discharge current density surfaces are shown in Fig. 4 for two oscillatory modes. The azimuthal (Az.) locations on the thruster are shown as numbered locations corresponding to an analog clock to prevent confusion about which direction is clockwise when viewing the thruster. The top of the thruster is 12 o'clock and the bottom of the thruster is 6 o'clock. The surface plot is j_D in units of mA/cm² and 1 ms time segments are shown. Vertical features represent extremes in discharge current density that occur everywhere in the channel simultaneously. Diagonal features are perturbations in discharge current density that propagate azimuthally around the discharge channel. Lines from upper-left to lower-right are propagating counterclockwise around the discharge channel, which is the $E \times B$ direction in the H6. Figure 4a shows local mode oscillation where the azimuthal spokes shown Fig. 3 are present and seen to propagate counterclockwise around the discharge channel in 0.3–0.4 ms or at a rate of ~1 deg/μs. Figure 4b shows global mode oscillation where the plasma in the entire discharge channel fluctuates in unison. Approximately 8.5 cycles are observed in 1 ms, corresponding to a frequency of ~8.5 kHz. Local and global oscillation mode will be defined in Sec. V.A. A 2-D Fourier transform of the spoke surface yields the spoke surface power spectral density (SS-PSD) for all spoke orders m. For $m > 1$, the spoke order corresponds to the number of spokes present in the discharge channel (e.g., an $m = 3$

Table 1 Test matrix showing discharge voltage and anode flow rate variations for internal cathode configuration[a]

	14.7 mg/s	19.5 mg/s	25.2 mg/s
300 V	1	4	2
400 V	— —	2	— —
450 V	— —	1	— —

[a]Number indicates the number of sweeps at the condition.

spoke order indicates three bright regions and three dark regions propagating in the channel).

IV. Results

A. Introduction

Mode transitions are observed during magnetic field sweeps across the range of operating conditions shown in Table 1. The two primary modes identified here are the low-oscillatory local mode and highly oscillatory global mode, which are defined in Sec. V.A. Metrics are developed to clearly identify the mode transition region and the difference between the highly oscillatory mode and unstable mode is discussed. The response of the discharge current and discharge current density in the discharge channel to mode transitions are characterized. Thruster performance changes through mode transitions are quantified.

B. Identification of Mode Transitions

1. Magnetic Field Sweeps

Magnetic field sweeps were typically started from $B_r/B_r^*|_{\max}$ and decreased until the thruster discharge was unstable, as indicated by an uncontrolled increase or "run-away" discharge current. Figure 5 shows a typical magnetic sweep at 300 V, 19.5 mg/s, lasting less than 1 h with approximately 3 min at each setting. The continuously recorded values for inner magnet current I_{IM} and mean discharge current $\bar{I}_D$ are shown with the discrete values used in later plots, identified as symbols. Inner magnet current, which is related to through Eq. (5), is decreased from the max of $I_{IM} = 5.5$ A in discrete steps until the thruster becomes unstable at $I_{IM} = 1.65$ A. To ensure thermal equilibrium, the thruster was operated for a minimum of 3 h before conducting magnetic field sweeps, and when changing conditions (discharge voltage or flow rates), it was operated for 0.5–1 h before sweeps. All xenon mass flow rates at 300 V discharge voltage were repeated during different vacuum chamber pumpdowns where the thruster was exposed to atmosphere between tests, yielding similar results.
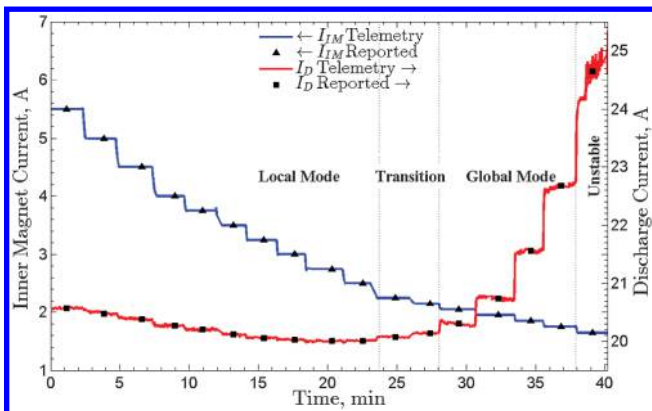

Fig. 5 Telemetry for (right axis) discharge current and (left axis) inner magnet current for a magnetic field sweep at 300 V, 19.5 mg/s recorded at 1 Hz. Reported values used in Figs. 6a and 7a are shown as symbols. B_r/B_r^* regions of local mode, global mode, and unstable operation are noted.

2. Highly Oscillatory Versus Unstable Operation

A distinction needs to be drawn between highly oscillatory operation (defined later as global oscillation mode) and unstable operation, which is often confused in the literature. An increase in mean discharge current and oscillation amplitude is often labeled as unstable operation; however, the thruster shows no sign of run-away behavior. Here, unstable operation is defined as the condition where discharge current begins to rise uncontrollably at a constant B_r/B_r^*. In Fig. 5, I_{IM} is decreased from the max of 5.50 A, where the thruster is in a low-oscillatory mode (defined later as local oscillation mode), until the thruster becomes unstable at 1.65 A. From $I_{IM} = 5.50$ until 2.25 A, the thruster is in local mode and transitions to global mode between 2.25 and 2.10 A. From $I_{IM} = 2.25$ to 1.75 A, the thruster is more oscillatory in global mode, but is stable at higher mean discharge current values. For $I_{IM} < 1.75$ A, the discharge current begins to steadily rise at ~1 A/min and significant fluctuations are seen even on the 1 Hz telemetry in Fig. 5, without any thruster setting changes until the test is terminated, which is unstable operation.

C. Discharge Current Response to Mode Transition

Although varying magnetic field magnitude with constant flow rate and discharge voltage, decreasing B_r/B_r^* below a certain threshold was shown to repeatedly induce a mode transition similar to those discussed in Sec. II where the mean discharge current increased and the discharge current amplitude increased. This was shown consistently for the three different voltages (300, 400, and 450 V) and three different flow rates (14.7, 19.5, and 25.2 mg/s) as shown in Figs. 6 and 7 where the plots of $\bar{I}_D$ and $\tilde{I}_D/\bar{I}_D$ versus B_r/B_r^* show two distinct regions with a transition region. The thruster is considered to be more susceptible to mode transitions if the transition $B_r/B_r^*|_{trans}$ occurs at higher B_r/B_r^* values. Because $B_r/B_r^*|_{max}$ is an upper limit due to thruster design, if the transition point occurs at higher B_r/B_r^*, then the range of magnetic field values where the thruster operates in local mode is diminished. The estimated uncertainty in transition point is ± 0.1 A for I_{IM} which corresponds to ± 0.03 for $B_r/B_r^*|_{trans}$.

Figures 6 and 7 show that increasing discharge voltage or flow rate increases the B_r/B_r^* where mode transition occurs. The transition points from Figs. 6 and 7 have been summarized in a later figure to highlight the trends. Figures 6a and 6b show the discharge current mean value and oscillation amplitude, respectively, for discharge voltages of 300, 400, and 450 V. The parenthetical numbers in the legend show the number of sweeps where the 300 V condition was repeated four times (one sweep was a continuous decreasing then increasing sweep) and the 400 V condition was repeated twice. The different sweeps showed remarkable consistency with deviations less than 3% of the mean, indicating the transitions were not caused by transient thruster properties such as outgassing or thermal nonequilibrium. Figure 7 shows that increasing anode flow rate with a constant 7% cathode flow fraction also increases the B_r/B_r^* where mode transition occurs. Figures 7a and 7b show the discharge current mean and oscillation amplitude, respectively, for anode flow rates of 14.7, 19.5, and 25.2 mg/s. The higher discharge voltages of 400 and 450 V in Fig. 6 showed a steadily increasing oscillation amplitude as B_r/B_r^* was increased for $B_r/B_r^* \geq 1$, yet the mean discharge current remained the same. Additionally, the lowest flow rate case of 14.7 mg/s for 300 V showed significantly higher oscillation amplitude in Fig. 7 for $B_r/B_r^* > 1.2$ than the other flow rates and requires further investigation.

D. Discharge Channel Current Density Response to Mode Transition

Figure 8 shows the discharge current and oscillation amplitude (top plot), the discharge current density surface, and SS-PSD plots from HIA for an example mode transition during a magnetic field magnitude sweep at the 300 V, 19.5 mg/s operating condition. A distinct change in discharge channel oscillations is observed in Fig. 8 with a transition point of $B_r/B_r^* = 0.61$. Several important features can be distinguished on the discharge current density surface plots, beginning with the low magnetic field setting of $B_r/B_r^* = 0.52$. Vertical stripes of constant current density indicates the entire discharge channel is acting in unison with minimal azimuthal
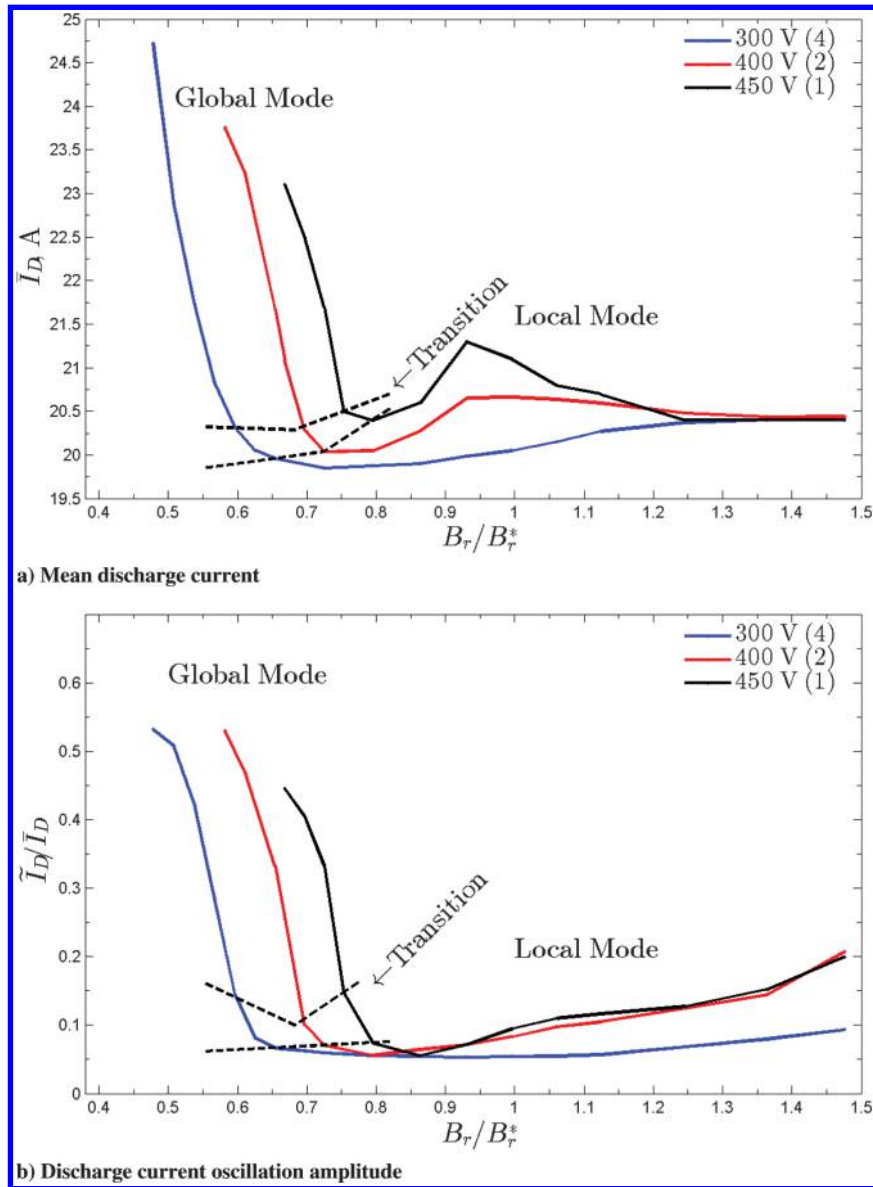
Fig. 6 Discharge current a) mean and b) oscillation amplitude variation with constant 19.5 mg/s anode flow rate and variable discharge voltages of 300, 400, and 450 V. Upper and lower bounds for transition region are shown. Number in parenthesis is number of sweeps averaged together.

nonuniformities, as shown clearly in $B_r/B_r^* = 0.52$. The fluctuations are large with the entire discharge channel at 70 mA/cm^2 (10.6 A) or approximately half of the nominal value at the minima and then rising to over 300 mA/cm^2 (45 A) during the peak. In 1 ms of the discharge current density surface shown in Fig. 8, 8.5 cycles are visible. This corresponds to a frequency of 8.5 kHz, which is clearly seen as a peak for $m = 0$ in the SS-PSD with corresponding harmonics at 17 and 25.5 kHz. No spokes are observed to have any significant peaks for $B_r/B_r^* = 0.52$. The SS-PSD peak in m_0 is over 10^7, which is two orders of magnitude higher than at the transition point ($B_r/B_r^* = 0.61$) or higher B_r/B_r^* values.

At the transition point, $B_r/B_r^* = 0.61$ in Fig. 8, strong vertical stripes are seen between 0.46 and 0.73 ms as well as 0.9 ms, indicating an oscillation in the entire channel from 110 to 160 mA/cm^2. These entire channel oscillations are significantly lower than the global oscillations seen at $B_r/B_r^* = 0.52$. The three oscillations seen between 0.46 and 0.73 ms correspond to 11 kHz oscillations. However, diagonal stripes are clearly visible from 0 to 0.4 ms with oscillations between 120 and 150 mA/cm^2, which are symmetric about the mean of 133 mA/cm^2 for the discharge current of 20 A. These diagonal stripes represent azimuthal spokes propagating around the channel counterclockwise, which is the $E \times B$ direction for the H6. The spokes extend for one-quarter to one-half

of the discharge channel before dissipating, and last from 100 to 200 μs in duration. The existence of spokes and global channel oscillations simultaneously indicates the thruster is switching or "bouncing" between the different oscillatory modes. The SS-PSD shows the magnitude of the global mode has decreased by two orders of magnitude and is now the 11 kHz noted earlier. Spoke orders $m = 3–6$ are present, with 4 and 5 the most dominant at 13 and 18 kHz, respectively.

For the reference magnetic field of $B_r/B_r^* = 1.00$ in Fig. 8, very few global oscillations are seen, as evidenced by the very flat m_0 in the SS-PSD, and only hints of vertical lines in the spoke surface. Spoke orders $m = 3–6$ are also present with 4 and 5 still the most dominant, but they have shifted down to 10 and 15 kHz, respectively. The spokes are stronger as evidenced by the higher SS-PSD peaks, but the length of the diagonal lines in the spoke surface has also increased. Spokes typically propagate over one-half to sometimes even the entire discharge channel, lasting for several hundred microseconds. The local oscillations represented by spokes are from 115 to 150 mA/cm^2, which is about the mean of 133 mA/cm^2 or 20 A.

For the high magnetic field of $B_r/B_r^* = 1.48$ in Fig. 8, the entire discharge channel occasionally oscillates in unison or "flickers" (i.e., 0.35 and 0.65 ms), but is not nearly as periodic as $B_r/B_r^* = 0.52$. The
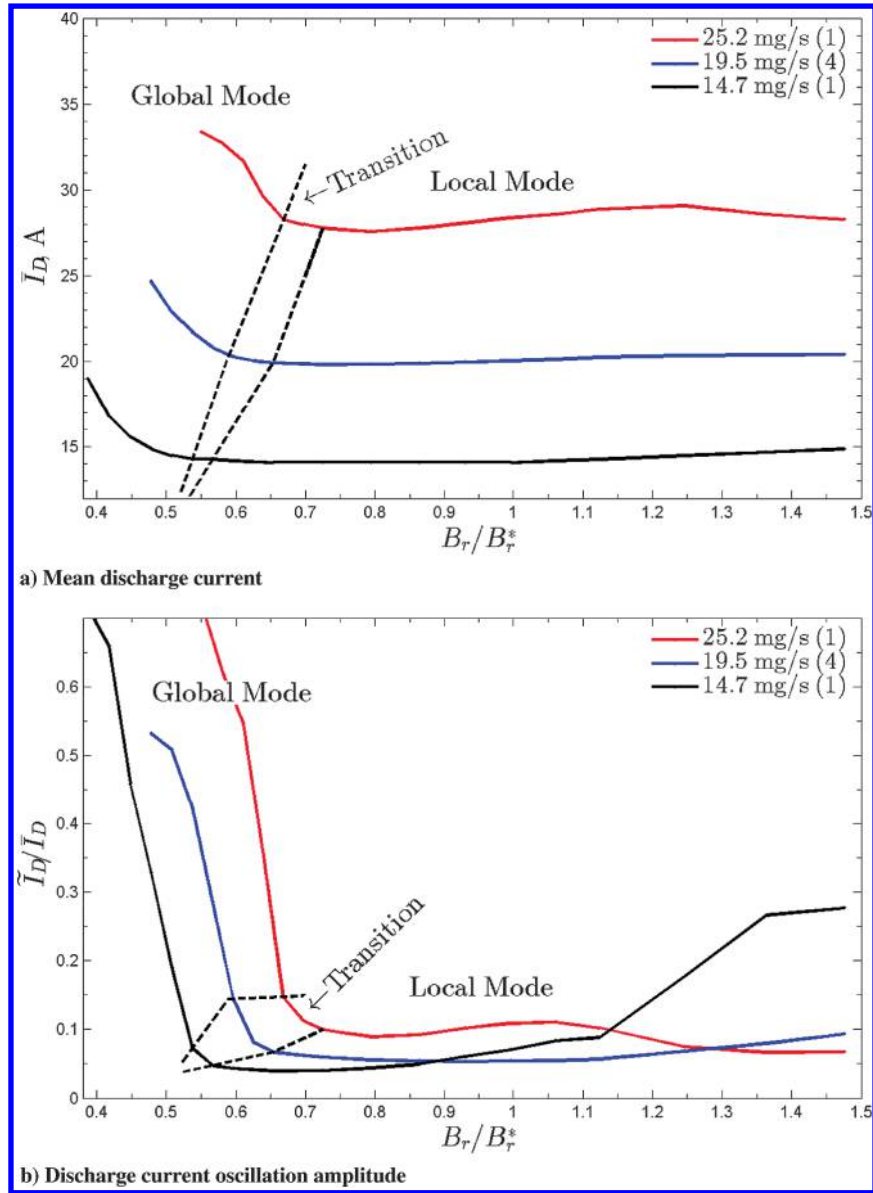
Fig. 7   Discharge current a) mean and b) oscillation amplitude variation with constant 300 V discharge and variable anode flow rates of 25.2, 19.5, and 14.7 mg/s. Upper and lower bounds for transition region are shown. Number in parenthesis is number of sweeps averaged together.

current density during these peaks can be as high as 180 mA/cm². Therefore, the m_0 mode is stronger than at $B_r/B_r^* = 1.00$, but the SS-PSD peak is much broader than at $B_r/B_r^* = 0.60$ or 0.51 because the flicker is more sporadic and not at one frequency. The spoke orders $m = 4$–8 are nearly the same level, with 4 and 5 shifting down again to 9 and 14 kHz, respectively. The spoke peaks are an order of magnitude lower than $B_r/B_r^* = 1.00$, indicating weaker spokes. As seen qualitatively in the spoke surface, the spokes are shorter in duration and so more spokes are present (higher spoke order), but propagate for shorter periods (lower SS-PSD peaks).

In summary, magnetic fields below the transition thresholds do not support spoke propagation or local oscillations and the entire discharge channel oscillates in unison. At the transition points, spokes are able to propagate but the channel occasionally reverts to global oscillation mode. At the reference magnetic strength of $B_r/B_r^* = 1$, spokes that are able to propagate over large regions of the discharge channel dominate and global oscillations are minimized. For higher magnetic field strengths, more spokes are present (higher m number in plots), but are less stable (occur for less time before disappearing in spoke surface). As the magnetic field increases, the peak frequency of each spoke order decreases, which

supports an inverse relation between the spoke frequency and magnetic field as noted in [11,25].

E.   Mode Transition Criteria

The example mode transition in Fig. 8 for the 300 V, 19.5 mg/s operating point can be used to describe mode transition criteria. The plasma in the entire discharge channel is oscillating in unison or global mode for $B_r/B_r^* = 0.52$ in Fig. 8, which is evidenced by the vertical stripes in the discharge current density plot. As the magnetic field magnitude is increased, the transition point $B_r/B_r^*|_{\text{trans}}$ at $B_r/B_r^* = 0.58$ is qualitatively identified when the entire channel plasma oscillations begin to break up, become irregular, and spokes intermittently form. The upper bound of the transition region is when the diagonal stripes indicative of azimuthal spokes dominate at $B_r/B_r^* = 0.65$, while still intermixed with sporadic vertical stripes of entire channel oscillations. Mode transition is complete when the azimuthal spokes dominate for $B_r/B_r^* \geq 0.73$, which is local oscillation mode. The thruster is operating in local mode for $B_r/B_r^* = 1.00$ and 1.48 in Fig. 8.

The discharge current and SS-PSD can be used to define quantitative transition criteria from global mode to local mode as
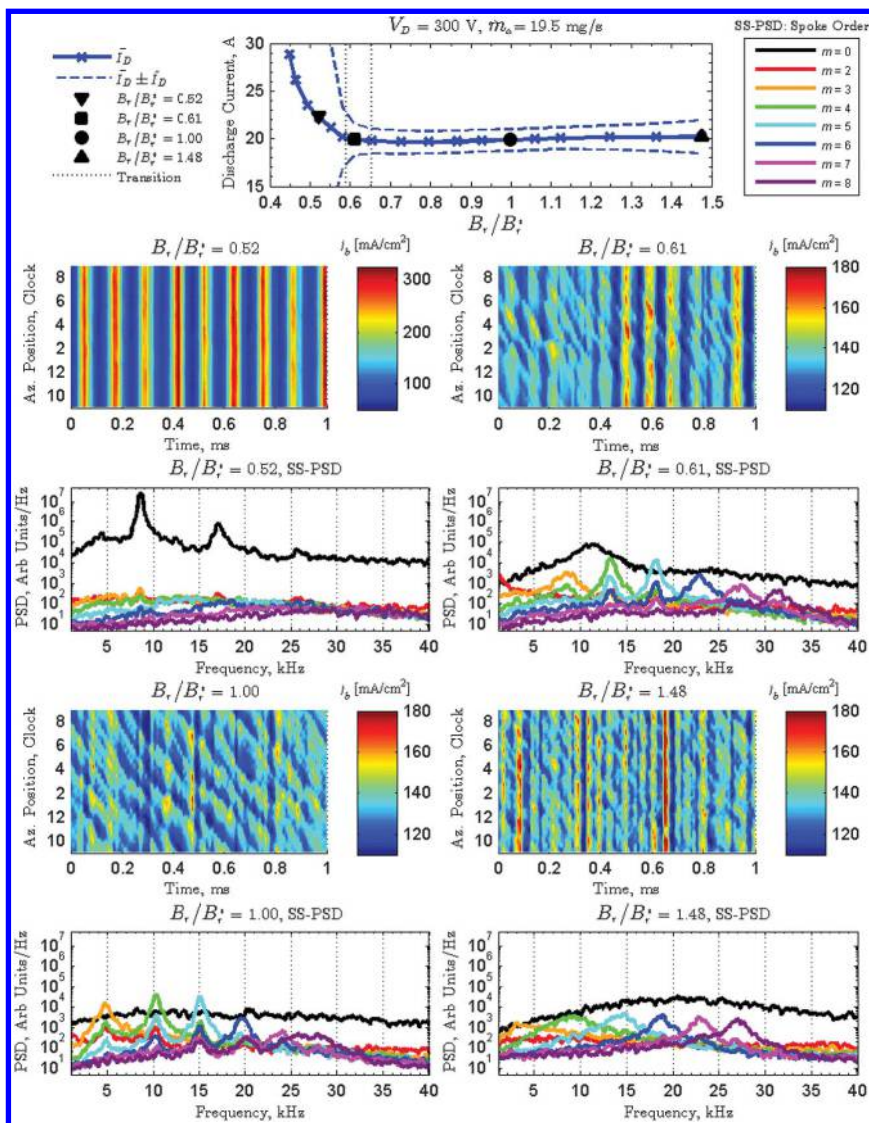
Fig. 8 Magnetic field sweep for 300 V, 19.5 mg/s showing transition at $B_r/B_r^* = 0.61$. Discharge current mean and oscillation amplitude are shown with the transition and for B_r/B_r^* settings selected for further analysis. Middle row plots are HIA PSDs and bottom row plots are discharge current density. The scale range for $B_r/B_r^* = 0.52$ discharge current density is larger due to the magnitude of oscillations. A 500 Hz moving average filter has been applied to smooth all PSDs.

listed in Table 2. $\mathrm{PSD}_{m_{\max}}$ is the peak SS-PSD for any spoke order $m > 1$, PSD_{m_0} is the peak for $m = 0$, and $\bar{I}_{D_{\min}}$ is the minimum mean discharge current during the sweep. The criteria of Table 2 are guidelines based on measurements in one thruster and not absolute cutoffs, however, these same techniques can be used to define transition criteria in similar thrusters. The transition point is associated with the destabilization of global mode because that is typically the clearest to identify, which marks the lower limit of the transition region ($I_{\mathrm{IM}} = 2.10$ A in Fig. 5). The upper limit of the transition region where the spokes dominate and global oscillations are absent or negligible is less distinct. The strong global oscillations begin to lose coherency at $B_r/B_r^*|_{\mathrm{trans}}$, but the plasma oscillations are typically seen to alternate between global mode and local mode for $B_r/B_r^*|_{\mathrm{trans}} \leq B_r/B_r^* \lesssim 1.1 B_r/B_r^*|_{\mathrm{trans}}$. This is considered the transition region where the discharge channel displays both oscillatory modes.

F. Performance Response to Mode Transition

The discharge power is $P_D = I_D V_D$, and thrust to power T/P and anode efficiency η_a are defined as [30]

$$T/P = \frac{T}{P_D} \qquad (6)$$

$$\eta_a = \frac{T^2}{2\dot{m}_a P_D} \qquad (7)$$

where $\dot{m}_a$ is the anode mass flow rate. Figure 9 shows the discharge current, thrust, thrust to power, and anode efficiency during magnetic field sweeps at 300 V. The mean thrust in Fig. 9b was 281, 379, and 507 mN for 14.5, 19.5, and 25.2 mg/s, respectively. The peak thrust to power in Fig. 9c was 67, 64, and 61 mN/kW and the peak anode efficiency in Fig. 9d was 65, 64, 63, and 63% for 14.5, 19.5, and 25.2 mg/s, respectively. The uncertainty on the thrust measurements, shown as error bars in Fig. 9b for the 14.7 and 25.2 mg/s case, is conservatively estimated to be 7 and 10 mN, respectively. Unfortunately, for the 19.5 mg/s case, a zero point was not acquired after the thruster reached equilibrium and before data acquisition, but a zero was acquired immediately after data acquisition. For this condition, B_r/B_r^* was decreased from 1.48 through mode transition and then increased back to 1.48. The discharge current during the downsweep and upsweep had a less than 4% difference at any one point in global mode and less than 1% difference at any one point in local mode, as shown in Fig. 9a. Therefore, the zero before data acquisition was estimated using the post-data-acquisition zero with the assumption that the thrust was the same for the downsweep and upsweep similar to discharge current, with a conservatively estimated

Table 2 Transition criteria between global and local oscillation mode for H6 based on SS-PSD and discharge current PSD

Criteria	Global mode	Local mode
$\frac{\text{PSD}_{m_0}}{\text{PSD}_{m_{\max}}}$	$\gtrsim 50$	$\lesssim 10$
$\tilde{I}_D/\bar{I}_D$	$\gtrsim 0.15$	$\lesssim 0.10$
$I_{D_m} = \frac{\bar{I}_D - \bar{I}_{D\min}}{\bar{I}_{D\min}}$	$\gtrsim 0.02$	$\lesssim 0.02$

20 mN uncertainty. As shown in Fig. 9b, this yielded a constant thrust throughout the sweeps in local and global mode to within 3%. For the 14.7 mg/s condition, the mean value was constant within experimental uncertainty for the entire magnetic field sweep. The thrust for the 25.2 mg/s condition increased with decreasing magnetic field from 482 to 518 mN, which is a ~7% change. Figure 9b shows that the thrust was not affected by mode transition. Zero points were appropriately taken before and after the magnetic field sweeps, and so the increase in thrust is likely not a thermal drift.

Figure 9d shows that, from $B_r/B_r^*|_{\text{trans}}^{\text{lower}}$, the anode efficiency for 14.7 mg/s decreases from 64 to 48%, for 19.5 mg/s decreases from 62 to 50%, and for 25.2 mg/s decreases from 62 to 53%. Although significant, these numbers are a worst case because the percentage decrease is related to how deep into global mode the thruster is operated. The most important aspect of this analysis is the observation in Figs. 9c and 9d that the peak in thrust to power and anode efficiency typically occurs at B_r/B_r^* just larger than $B_r/B_r^*|_{\text{trans}}^{\text{upper}}$ and not the reference magnetic field setting of $B_r/B_r^* = 1$. Therefore, thruster performance is typically maximum near the transition point, but once the thruster transitions from local mode to global mode, the performance decreases significantly with a further decrease in B_r/B_r^*.

V. Discussion

A. Definition of Modes

The general shape shown in the previous work in Fig. 1 is repeatedly demonstrated, but the description of oscillations and regimes are significantly different. Additionally, the shape of the discharge current trace for oscillating and pulsed mode in the SPT-100ML [4] are similar to the global mode discussed in this work, as well as the marked increase in discharge current and decrease in thruster efficiency. The shape of the discharge current time history in region C, identified by Tamida et al. [3], between the classical diffusion region and Bohm diffusion region qualitatively resembles the discharge current characteristics for global oscillation mode in this investigation. The different modes of HET operation are defined in the present work by their plasma oscillation characteristics, where most conditions should be satisfied to represent either mode. An attempt is made to quantify the mode metrics, but the criteria values are meant only as a guide and not rigid discriminators. These criteria are based on the preceding observations of the H6 and are likely different for other HETs, but because mode transitions have been observed in other thrusters, a subset of the following criteria should apply. These definitions delineate the thruster behavior when in either mode, but a less defined transition region exists from $B_r/B_r^*|_{\text{trans}}^{\text{lower}}$ to $B_r/B_r^*|_{\text{trans}}^{\text{upper}}$. In this transition region, the thruster does not meet all of the criteria for either mode and the HIA clearly shows the thruster jumping between modes, as evidenced from $B_r/B_r^* = 0.61$ in Fig. 8.

1. Global Mode

The discharge current density in the entire channel is oscillating in unison with peak values of order 100% of the mean value, and azimuthally propagating perturbations are either entirely absent or of negligible magnitude with respect to the discharge current density peaks. The m_0 mode of the SS-PSD has a clearly defined peak value and spoke orders $m \geq 2$ do not have peaks more than an order of magnitude above the general noise floor. The discharge current oscillation amplitudes (rms) are well above 10% of the mean discharge current value, and the mean discharge current is over 15% higher than the minimum discharge current value obtained in a sweep. Additionally, azimuthally spaced ion saturation reference probes do not observe delays in plasma property oscillations indicative of the entire channel luminosity or current density oscillating in unison and are well correlated to the discharge current [26]. An ion saturation reference probe is an electrostatic probe maintained at a continuous negative bias for time-resolved ion saturation measurements. Sekerak et al. [31] used them to augment high-speed dual Langmuir probes for time-resolved plume measurements.
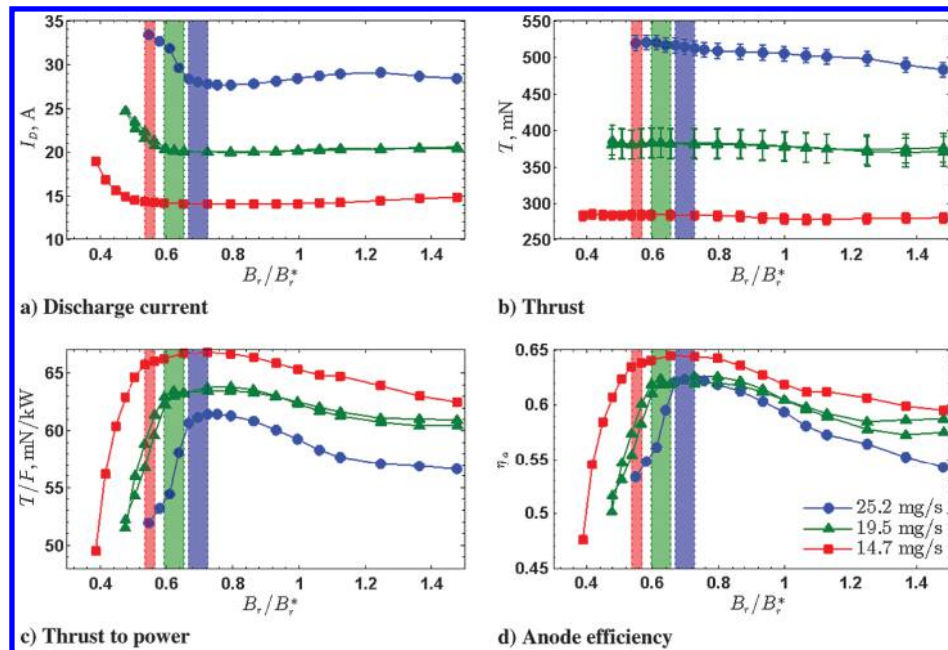

Fig. 9 Discharge (330 V) and anode flow rates of 25.2 (blue), 19.5 (green), and 14.7 (red) mg/s: a) discharge current, b) thrust, c) thrust to power, and d) anode efficiency. Shaded regions are the transition regions for a particular anode mass flow rate. Error bars on thrust measurements in Fig. 9b are estimated uncertainties.

2. Local Mode

The discharge current density oscillations are dominated by localized perturbations that are less than 25% of the mean value and propagate in the $E \times B$ direction. Oscillations may be present where the entire channel luminosity or discharge current increases or decreases in unison, but they are sporadic and do not dominate the azimuthal propagations. The m_0 mode of the SS-PSD has a very broad peak value and spoke orders $m \geq 2$ have peaks more than an order of magnitude above the general noise floor. The discharge current oscillation amplitudes (rms) are less than approximately 10% of the mean discharge current value, and the mean discharge current is within 15% of the minimum discharge current value obtained in a sweep. The discharge channel and near-field plume regions are observed to be dimmer, indicative of decreased collisions in the plume and collisional processes more confined to within the discharge channel. Additionally, azimuthally spaced ion saturation reference probes observe clear delays in plasma property oscillations, indicating localized regions of increased ionization moving counterclockwise within the discharge channel propagating downstream, and the probe signals are not well correlated to the discharge current [31].

3. Transition Point Characterization

Figures 6 and 7 show that mode transition occurs at higher magnetic field strength for increasing discharge voltage and mass flow rate. The lower limit of the transition region $B_r/B_r^*|_{trans}^{lower}$ is plotted versus anode mass flow rate and discharge voltage in Fig. 10. A power law can be used to relate $B_r/B_r^*|_{trans}^{lower}$ to V_D and $\dot{m}_a$ with the form

$$B_r/B_r^*|_{trans}^{lower} = C\left(\frac{V_D}{V_D^*}\right)^\beta \left(\frac{\dot{m}_a}{\dot{m}_a^*}\right)^\gamma \tag{8}$$

where C is a linear coefficient, β and γ are exponents, and V_D^* and $\dot{m}_a^*$ are constant reference values. Equation (8) can be written in matrix form and the coefficients solved using a Moore–Penrose pseudoinverse matrix with the data in Fig. 10, which is the least-squares solution to the overdetermined problem:

$$B_r/B_r^*|_{trans}^{lower} = 0.593\left(\frac{V_D}{V_D^*}\right)^{0.4}\left(\frac{\dot{m}_a}{\dot{m}_a^*}\right)^{0.5} \approx 0.6\sqrt{\left(\frac{V_D}{V_D^*}\right)\left(\frac{\dot{m}_a}{\dot{m}_a^*}\right)} \tag{9}$$

A "transition surface" can also be plotted using Eq. (9), as shown in Fig. 11. More testing is required to validate the accuracy of the transition surface over the entire range, but the surface in Fig. 11 demonstrates a new technique for defining the operational modes of an HET. Using experimental data or an empirical relation, the transitions points can be determined a priori over a prescribed range of discharge voltages and mass flow rates to avoid thruster operation near those settings.

Equation (9) shows that $V_D \dot{m}_a/B_r^2 = $ const is a transition line similar to the classical diffusion line shown by Tamida et al. [3]. However, $V_D \dot{m}_a/B_r^2 < $ const transitions from small-amplitude oscillation in region B to large-amplitude oscillations in region C in [3], whereas in this investigation, the transition is from large-amplitude global mode oscillations to small-amplitude local mode oscillations. This difference requires further investigation and may be the result of different thruster design or magnetic field topology.

To theoretically investigate the physics behind the transition, Eq. (9) should be formulated as a function of quantities that appear in continuity equations. The ion velocity can be related to the discharge potential using conservation of energy

$$V_D = \frac{m_i v_i^2}{2q\eta_v} \tag{10}$$

where the voltage utilization efficiency η_v is the fraction of the discharge potential the average ion is accelerated through. The mass flux of particles through the discharge channel of area A_{ch} is

$$\dot{m} = A_{ch} n_N m_N v_{th_N} \tag{11}$$

where n_N is the neutral particle density and $v_{th_N} = \sqrt{8k_B T_N/(\pi m_N)}$ is the thermal velocity for neutrals of temperature T_N in Kelvin and mass m_N. Using Eqs. (10) and (11), Eq. (9) can be written as

$$B_r/B_r^*|_{trans}^{lower} \approx \Psi v_i \sqrt{n_N v_{th_N}} \tag{12}$$

$$\Psi = 0.6 m_i \sqrt{\frac{A_{ch}}{2V_D^* \dot{m}_a^* q\eta_V}} \tag{13}$$

Equation (12) shows that the transition point scales linearly with ion velocity and as the square root of neutral density and neutral velocity for the very limited number of data shown in Fig. 11. More data are required over a large range of V_D and $\dot{m}_a$, but the techniques presented here, especially the idea of a transitions surface, are still valid. These relations do not elucidate the underlying physics behind
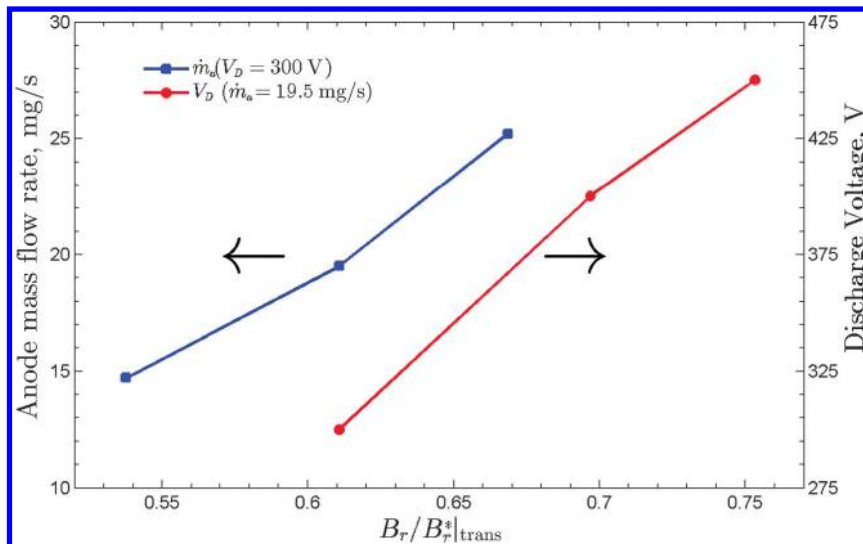

Fig. 10   Mode transition point as a function of (left axis) anode flow rate at constant discharge voltage (300 V) and (right axis) discharge voltage at constant anode flow rate (19.5 mg/s). Lower bound of transition region is shown with an uncertainty in $B_r/B_r^*|_{trans}$ of ±0.03. Multiple sweeps for 300 and 400 V have been averaged together.
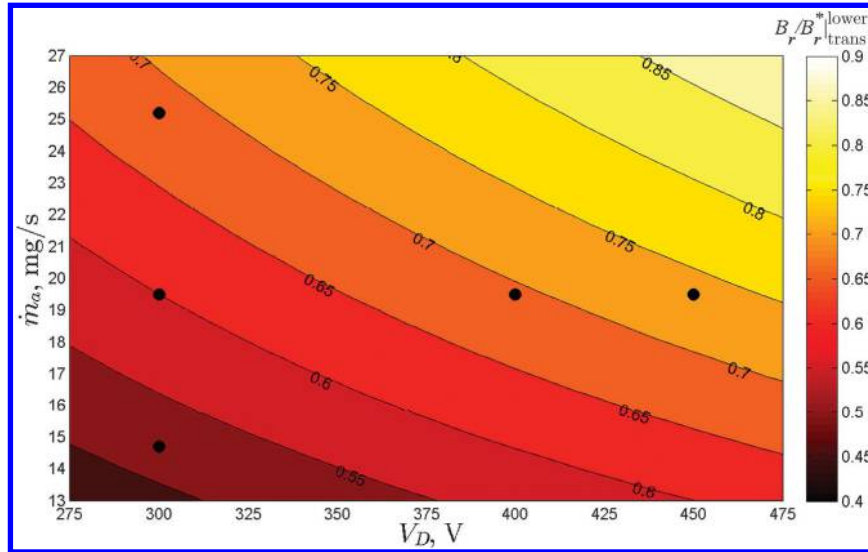
Fig. 11 Transition surface generated from the approximation in Eq. (9) for $B_r/B_r^*|_{\text{trans}}^{\text{lower}}$ for a range of discharge voltages and anode mass flow rates. Black dots represent the conditions tested in Table 1.

mode transitions and are only meant as characterization methods for thruster operation as a function of parameters similar to [3]. However, recent work by Hara et al. to understand the physics of mode transitions shows that electron transport across magnetic field lines and electron energy balance, including joule heating and wall losses, are critical for mode transitions [12,29].

B. Impact to Thruster Characterization

Figures 9c and 9d clearly show that T/P and anode efficiency decrease for $B_r/B_r^* < B_r/B_r^*|_{\text{trans}}^{\text{lower}}$ where the thruster has transitioned from local mode to global mode. The 25% decrease in thrust to power during mode transition for the 14.7 mg/s case was similar to the results of the low-voltage investigation of Brown and Gallimore [9]. The minimum mean discharge current typically occurred in local mode right before the transition region, as shown in Figs. 6 and 7. Similarly, the peak T/P and anode efficiency occurs near the transition point in Fig. 9, where the thruster is on the verge of entering global oscillation mode. If an operator were to choose magnetic field settings for flight operation based on maximizing T/P or minimizing $\bar{I}_D$, then the thruster would be operating near the transition point, where any perturbation in magnetic field (due to pole piece B-H properties changing over time, magnetic coils degrading, etc.) or changes in wall geometry and properties (due to erosion, coating from sputtered material, etc.) during the mission could cause the thruster to be more susceptible to transitioning from local oscillation mode to global oscillation mode. The magnetic field sweeps shown in Figs. 6 and 7 were constant and repeatable across several pumpdowns, but will likely change during the life of the thruster. This is more likely to be true if the transitions are related to wall effects, where the plasma properties near the wall (i.e., susceptibility to space charge saturation) may change as the wall erodes. Therefore, discharge current versus magnetic field curves, although very repeatable during this test campaign, are likely only snapshots and may change after thousands of hours of operation. The most important take away from this investigation is a new perspective on performance mapping of thrusters. Figure 10 shows that the transition point occurs at higher magnetic field magnitude for increased anode flow rate or discharge voltage. Discharge current versus discharge voltage mapping ($I_D - V_D$) are commonly performed on thrusters at beginning of life or after thousands of hours of operation. However, more insight into thruster performance and stability margins is gained by also mapping magnetic field to generate or $I_D - V_D - B$ maps, as shown in Fig. 12, to identify the mode transition boundaries. This can be done for different flow rates, cathode flow fractions, or different facility background pressures over the entire range of I_D and V_D to understand the regions of thruster stability demonstrated recently in

[10]. Using these results, it can be assured that thrusters are not operated near a transition point, where the thruster unintentionally enters global oscillation mode and decreases thruster performance. In general, mode transitions caused by magnetic field changes will occur at higher magnetic field strengths for higher mass flow rate or higher discharge voltage. There can be many causes for mode transition besides magnetic field variations used in this investigation, including cathode flow fraction variations. Based on Brown and Gallimore's work for low-voltage operation [9], the thruster is more sensitive to mode transitions caused by cathode flow fraction changes for lower mass flow rate or lower discharge voltage. Because thrust is constant or nearly constant, the increased discharge current is almost entirely excess electron current to the anode. This is supported by low-voltage H6 operation in Brown and Gallimore's work ([9] Table 2), where the current utilization efficiency decreased as little as 0.04 to as much as 0.1 from low- (local) to high-current (global) mode.

As the magnetic field is decreased, the cross-field resistivity decreases, therefore, increased current across the magnetic field lines is expected. However, the mode transition marks a percentage of discharge current increase that is disproportionate to the magnetic field decrease. Although the discharge current increase as magnetic field decreases is expected, the difference in plasma oscillations may be responsible for the significant increase in discharge current (i.e., increased electron transport across magnetic field lines). Consider the steady-state perpendicular velocity component from the electron fluid equation of motion and assume quasi neutrality, axisymmetry of the plasma in the discharge channel and purely axial electric field and purely radial magnetic field. Neglect ion current to the anode, so that the electron current density to the anode is approximately the discharge current density j_D, and neglect contributions from density and electron temperature gradients. Assume the axial electric field can be approximated as voltage utilization efficiency fraction of the discharge voltage divided by the ionization region length L_i, and the electron cyclotron frequency is much larger than the effective collision frequency ν_{ef}. The discharge current can be approximated as

$$I_D \sim \frac{A_{\text{ch}} m_e \eta_V V_D n \nu_{\text{ef}}}{L_i} \frac{1}{B_r^2} \quad (14)$$

Equation (14) shows that the discharge current would be expected to vary as $I_D \propto B_r^{-2}$ if ν_{ef}, n, and L_i are not functions of magnetic field strength. This relation of I_D to B_r is approximately valid in the global oscillation region of Figs. 6a and 7a, but in local oscillation mode, the discharge current is nearly constant or even increasing with increase
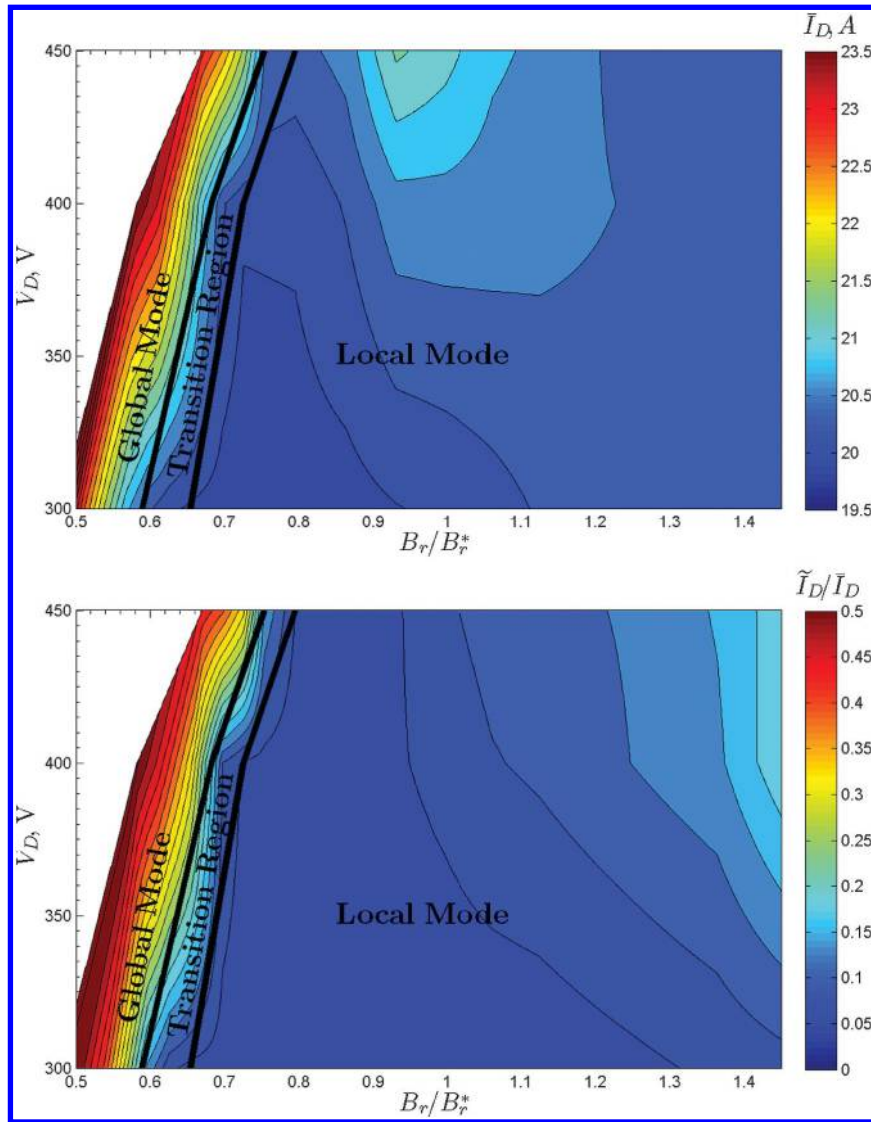
Fig. 12 Example $I_D - V_D - B$ surface for (top) I_D and (bottom) $\tilde{I}_D/\bar{I}_D$ generated from data in Fig. 6a for $V_D = 300$, 400, and 450 V. This graphic is meant to illustrate the utility of an $I_D - V_D - B$ plot to identify minimum discharge current, but is not intended for operational use because the data have been linearly interpolated between only three discharge voltages tested.

in magnetic field strength across a wide range of magnetic field values. This supports that electron transport mechanisms differ between the two oscillatory modes of thruster operation. In addition, a perturbation analysis that includes the electron energy equation shows that reduced electron transport and increased electron temperatures will stabilize ionization instabilities with energy loss to the wall [12]. Finally, hybrid-direct kinetic simulations suggest that reduced electron transport stabilizes the global oscillation mode, where joule heating balances other losses [29].

The body of research presented here underscores the importance of knowing where transition points are and how to control the mode of operation. A list of recommended improvements for thruster design and for more comprehensive thruster characterization to compare ground test performance to in-flight performance is as follows:

1) New thruster designs should have magnetic circuits with more capability and not be designed near saturation for the pole pieces. This will allow a wide range of variation in the magnetic field magnitude without altering the shape.

2) A transition surface should be empirically determined similar to Fig. 11 for a range of expected operating conditions. This should be performed at beginning of life and at regular intervals.

3) $I_D - V_D - B$ surfaces should be calculated for each flow rate, similar to Fig. 12. This should be performed at beginning of life and at

regular intervals. Determine the values of $\bar{I}_D$ and $\tilde{I}_D/\bar{I}_D$ that are representative of stable regions that can be used as metrics for thruster operation.

4) Each condition should be characterized on the ground by time-resolved diagnostics (high-speed probes and ultrafast imaging) to comprehensively understand the oscillatory characteristics. This will provide a large parameter space for thruster operation where the oscillations are characterized and correlated to discharge current (and any other diagnostics that are anticipated to be available in flight).

5) High-speed diagnostics will likely not be available on flight systems, but thruster oscillatory mode can be determined from time-resolved discharge current measurements in-flight. Build capability into the thruster power-processing unit to burst sample discharge current at ≥ 200 kHz for periods ≥ 10 ms. This will allow PSD calculations to quantify and characterize discharge current oscillations and compare with the detailed ground measurements.

VI. Conclusions

Previous researchers have identified mode transitions in HETs, where a small change in a thruster operating parameter such as discharge voltage, magnetic field, or mass flow rates causes the thruster discharge current mean and oscillation amplitude to increase significantly. Mode transitions in the H6 were induced by varying the

magnetic field intensity, while holding all other operating parameters constant, and measurements were acquired with ultrafast imaging. The modes are described here as global oscillation mode and local oscillation mode. In global mode, the entire discharge channel is oscillating in unison and spokes are either absent or negligible with discharge current oscillation amplitude (rms) greater than 10% of the mean value and can even be as high as 100%. In local oscillation mode, perturbations in the discharge current density are seen to propagate in the $E \times B$ direction with clear spokes shown in a SS-PSD. Spokes are localized oscillations that are typically 10–20% of the mean discharge current density value. The discharge current oscillation amplitude and mean values are significantly lower than global mode. The mode transitions were consistent across different tests, but did change at different operating conditions. The transition between global mode and local mode occurred at higher relative magnetic field strengths for higher mass flow rate or higher discharge voltage. The thrust was approximately constant through the mode transition, but the thrust-to-power ratio and anode efficiency decreased significantly in global mode. The peaks in thrust to power and anode efficiency typically occur near the transition point. Based on the research presented here, the H6 and likely any similar thruster should be operated in local oscillation mode to minimize discharge current and maximize performance. Thruster performance maps should include variation in discharge current, discharge voltage, and magnetic field, known as $I_D - V_D - B$ maps, at different flow rates to identify transition regions throughout the life of a thruster. These results are used to calculate a transition surface for use by operators to keep the thruster operating in an optimal mode. New thruster designs should have magnetic circuits with more capability and not be designed near saturation. These techniques are naturally extendable to comparing ground-test operation with on-orbit operation.

Acknowledgments

References

[1] Morozov, A. I., "The Conceptual Development of Stationary Plasma Thrusters," *Plasma Physics Reports*, Vol. 29, No. 3, March 2003, pp. 235–250.
doi:10.1134/1.1561119

[2] Tilinin, G. N., "High-Frequency Plasma Waves in a Hall Accelerator with an Extended Acceleration Zone," *Zh. Tekh. Fiz.*, Vol. 47, Aug. 1977, pp. 1684–1691.

[3] Tamida, T., Nakagawa, T., Suga, I., Osuga, H., Ozaki, T., and Matsui, K., "Determining Parameter Sets for Low-Frequency-Oscillation-Free Operation of Hall Thruster," *Journal of Applied Physics*, Vol. 102, No. 4, 2007, Paper 043304.
doi:10.1063/1.2771039

[4] Bechu, S., Perot, C., Gascon, N., Lasgorceix, P., Hauser, A., and Dudeck, M., "Operating Mode Investigation of a Laboratory Stationary Plasma Thruster," *35th Joint Propulsion Conference*, AIAA Paper 1999-2567, June 1999.

[5] Bechu, S., Lasgorceix, P., Gascon, N., Roche, S., Prioul, M., Albarede, L., and Dudeck, M., "Comparison Between Two Kinds of Hall Thrusters —SPT100 and ATON," *36th AIAA/ASME/SAE/ASEE Joint Propulsion*, AIAA Paper 2000-3524, 2000; also *36th Joint Propulsion Conference*, AIAA Paper 2000-3523, July 2000.

[6] Roche, S., Bechu, S., Prioul, M., Pagnon, D., Gascon, N., Bouchoule, A., Magne, L., Lasgorceix, P., and Touzeau, M., "Plasma Character-isation of an ATON-Hall Thruster– Channel and Plume Investigation," *31st International Electric Propulsion Conference*, Paper IEPC- 2009-074, Electric Rocket Propulsion Soc. (ERPS), July 2000, http://erps.spacegrant.org/.

[7] Gascon, N., Dudeck, M., and Barral, S., "Wall Material Effects in Stationary Plasma Thrusters. I. Parametric Studies of an SPT-100," *Physics of Plasmas*, Vol. 10, No. 10, 2003, p. 4123.
doi:10.1063/1.1611880

[8] Barral, S., Makowski, K., Peradzynski, Z., Gascon, N., and Dudeck, M., "Wall Material Effects in Stationary Plasma Thrusters II. Near-Wall and In-Wall Conductivity," *Physics of Plasmas*, Vol. 10, No. 10, 2003, p. 4137.
doi:10.1063/1.1611881

[9] Brown, D., and Gallimore, A., "Investigation of Low Discharge Current Voltage Hall Thruster Operating Modes and Ionization Processes," *31st International Electric Propulsion Conference*, Paper IEPC-2009-074, Electric Rocket Propulsion Soc. (ERPS), Sept. 2009, http://erps.spacegrant.org/.

[10] Brown, D. L., Blakely, J. M., and Lobbia, R. B., "Low-Voltage Hall Thruster Mode Transitions," AIAA Paper 2014-3510, July 2014.

[11] McDonald, M., and Gallimore, A., "Parametric Investigation of the Rotating Spoke Instability in Hall Thrusters," *32nd International Electric Propulsion Conference*, Paper IEPC-2011-242, Electric Rocket Propulsion Soc. (ERPS), Sept. 2011, http://erps.spacegrant.org/..

[12] Hara, K., Sekerak, M. J., Boyd, I. D., and Gallimore, A. D., "Perturbation Analysis of Ionization Oscillations in Hall Effect Thrusters," *Physics of Plasmas*, Vol. 21, No. 12, Dec. 2014, Paper 122103.
doi:10.1063/1.4903843

[13] Zhurin, V., Kahn, J., Kaufman, H., and Day, M., "Dynamic Characteristics of Closed Drift Thrusters," *23rd International Electric Propulsion Conference*, Paper IEPC-1993-095, Electric Rocket Propulsion Soc. (ERPS), Sept. 1993, http://erps.spacegrant.org/.

[14] Reid, B. M., Shastry, R., Gallimore, A. D., and Hofer, R. R., "Angularly-Resolved ExB Probe Spectra in the Plume of a 6-kW Hall Thruster," *44th AIAA/ASME/SAE/ASEE Joint Propulsion Conference and Exhibit*, AIAA Paper 2008-5287, July 2008.

[15] Haag, T. W., "Thrust Stand for High-Power Electric Propulsion Devices," *Review of Scientific Instruments*, Vol. 62, No. 5, 1991, p. 1186.
doi:10.1063/1.1141998

[16] Reid, B. M., "The Influence of Neutral Flow Rate in the Operation of Hall Thrusters," Ph.D. Dissertation, Univ. of Michigan, Ann Arbor, MI, 2009.

[17] Shastry, R., "Experimental Characterization of the Near-Wall Region in Hall Thrusters and Its Implications on Performance and Lifetime," Ph.D. Dissertation, Univ. of Michigan, Ann Arbor, MI, 2011.

[18] Xu, K. G., and Walker, M. L. R., "High-Power, Null-Type, Inverted Pendulum Thrust Stand," *Review of Scientific Instruments*, Vol. 80, No. 5, 2009, Paper 055103.
doi:10.1063/1.3125626

[19] Hofer, R., Goebel, D., Mikellides, I., and Katz, I., "Design of a Laboratory Hall Thruster with Magnetically Shielded Channel Walls, Phase II: Experiments," *48th AIAA/ASME/SAE/ASEE Joint Propulsion Conference & Exhibit*, AIAA Paper 2012-3789, Aug. 2012.

[20] Huang, W., "Study of Hall Thruster Discharge Channel Wall Erosion via Optical Diagnosticsm," Ph.D. Dissertation, Univ. of Michigan, Ann Arbor, MI, 2011.

[21] McDonald, M., "Electron Transport in Hall Thrusters," Ph.D. Dissertation, Univ. of Michigan, Ann Arbor, MI, 2012.

[22] Hofer, R. R., Goebel, D. M., Mikellides, I. G., and Katz, I., "Magnetic Shielding of a Laboratory Hall Thruster. II. Experiments," *Journal of Applied Physics*, Vol. 115, No. 4, Jan. 2014, Paper 043304.
doi:10.1063/1.4862314

[23] McDonald, M., Bellant, C., St Pierre, B., and Gallimore, A., "Measurement of Cross-Field Electron Current in a Hall Thruster Due to Rotating Spoke Instabilities," *47th AIAA/ASME/SAE/ASEE Joint Propulsion Conference & Exhibit*, AIAA Paper 2011-5810, Aug. 2011.

[24] McDonald, M. S., and Gallimore, A. D., "Rotating Spoke Instabilities in Hall Thrusters," *IEEE Transactions on Plasma Science*, Vol. 39, No. 11, Nov. 2011, pp. 2952–2953.
doi:10.1109/TPS.2011.2161343

[25] McDonald, M. S., and Gallimore, A. D., "Comparison of Breathing and Spoke Mode Strength in the H6 Hall Thruster Using High Speed Imaging," *33rd International Electric Propulsion Conference*, Paper IEPC-2013-353, Electric Rocket Propulsion Soc. (ERPS), Oct. 2013, http://erps.spacegrant.org/.

[26] Sekerak, M. J., "Plasma Oscillations and Operational Modes in Hall Effect Thrusters," Ph.D. Dissertation, Univ. of Michigan, Ann Arbor, MI, 2014.

[27] Sekerak, M. J., Longmier, B. W., Gallimore, A. D., Brown, D. L., Hofer, R. R., and Polk, J. E., "Azimuthal Spoke Propagation in Hall Effect

Thrusters," *IEEE Transactions on Plasma Science*, Vol. 43, No. 1, 2014, pp. 1–1.

[28] Lobbia, R., Liu, T., and Gallimore, A., "Correlating Time-Resolved Optical and Langmuir Probe Measurements of Hall Thruster Dynamics," *JANNAF 3rd Spacecraft Propulsion Joint Subcommittee Meeting*, SPS-III-36, Electric Rocket Propulsion Soc. (ERPS), Dec. 2008, http://erps.spacegrant.org/.

[29] Hara, K., Sekerak, M. J., Boyd, I. D., and Gallimore, A. D., "Mode Transition of a Hall Thruster Discharge Plasma," *Journal of Applied Physics*, Vol. 115, No. 20, May 2014, Paper 203304.
doi:10.1063/1.4879896

[30] Hofer, R. R., "Development and Characterization of High-Efficiency, High-Specific Impulse Xenon Hall Thrusters," Ph.D. Dissertation, Univ. of Michigan, Ann Arbor, MI, 2004.

[31] Sekerak, M. J., McDonald, M. S., Hofer, R. R., and Gallimore, A. D., "Hall Thruster Plume Measurements from High-Speed Dual Langmuir Probes with Ion Saturation Reference," *34th IEEE Aerospace Conference*, Big Sky, MT, March 2013.

J. Blandino
Associate Editor

This article has been cited by:

1. Jason D. Frieman, Nathan P. Brown, Connie Y. Liu, Thomas M. Liu, Mitchell L. R. Walker, Vadim Khayms, David Q. King. Impact of Propellant Species on Hall Effect Thruster Electrical Facility Effects. *Journal of Propulsion and Power*, ahead of print1-14. [Abstract] [Full Text] [PDF] [PDF Plus]

2. Yongjie Ding, Hongbo Su, Peng Li, Liqiu Wei, Hong Li, Wuji Peng, Yu Xu, Hezhi Sun, Daren Yu. 2017. Study of the catastrophic discharge phenomenon in a Hall thruster. *Physics Letters A* **381**:40, 3482-3486. [Crossref]

3. Sarah E. Cusson, Ethan T. Dale, Alec D. Gallimore. 2017. Investigation of Channel Interactions in Nested Hall Thruster. *Journal of Propulsion and Power* **33**:4, 1037-1040. [Citation] [Full Text] [PDF] [PDF Plus]